Blade-resolved and Actuator Line simulations of rotor wakes

André F.P. Ribeiro, Thomas Leweke, Aliza Abraham, Jens N. Sørensen, Robert F. Mikkelsen

Graphical Abstract

Blade-Resolved and Actuator Line Simulations of Rotor Wakes

André F. P. Ribeiro, Thomas Leweke, Aliza Abraham, Jens N. Sørensen, Robert F. Mikkelsen

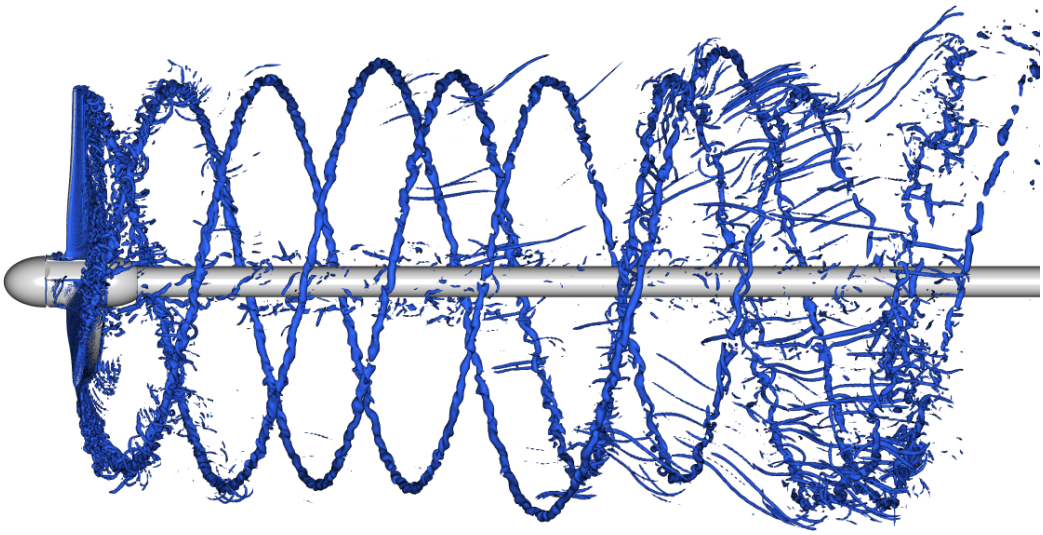

Highlights

Blade-Resolved and Actuator Line Simulations of Rotor Wakes

André F. P. Ribeiro, Thomas Leweke, Aliza Abraham, Jens N. Sørensen, Robert F. Mikkelsen

- Simulations of a three-bladed rotor in wind turbine configuration are done in a blade-resolved manner, with excellent agreement to experiments.
- The actuator line method is used for the same configuration and several limitations are highlighted.
- Preset actuator line simulations, with forces extracted from the blade-resolved case and an analytical model are performed and are shown to agree well with experiments.
- An asymmetric rotor is tested and the different methods are able to capture the earlier leapfrogging introduced by the asymmetry.

Blade-Resolved and Actuator Line Simulations of Rotor Wakes

André F. P. Ribeiro[a], Thomas Leweke[b], Aliza Abraham[b], Jens N. Sørensen[c], Robert F. Mikkelsen[c]

[a]*SIMULIA, Dassault Systemes GmbH, Stuttgart, 70563, Germany*
[b]*IRPHE, Aix-Marseille Université, CNRS, Centrale Méditerranée, Marseille, 13384, France*
[c]*DTU Wind and Energy Systems, Technical University of Denmark, Kongens Lyngby, 2800, Denmark*

Abstract

This work concerns high-fidelity numerical simulations of a rotor wake, with focus on the tip vortices and their stability. Blade-resolved and actuator line lattice-Boltzmann simulations are performed on a symmetric baseline rotor, as well as on a rotor with asymmetries. The asymmetry has the purpose of destabilizing the tip vortices to enhance wake recovery and hence the performance of potential downstream turbines. Limitations in the actuator line method are highlighted, and we show the potential of addressing these limitations with a so-called "preset" actuator line, where the forces are extracted from blade-resolved simulations, or an analytical load model, which as input only requires the thrust and power coefficients. Simulations agree well with experimental results and leapfrogging is captured, even with a coarse actuator line simulation. The asymmetric rotor is shown to improve power in the far-wake by 12%.

Keywords: Instability, wind turbine wake, leapfrogging

1. Introduction

The near wake of a wind turbine is formed by helical vortices shed from the tips and roots of the rotor blades [1]. These coherent vortices can cause increased fatigue loading on downstream turbines within a wind farm and delay wake recovery by blocking mixing between the low-speed flow inside the wake and the free-stream flow outside [2]. This delayed wake recovery

limits the minimum allowable spacing between turbines within a wind farm, reducing the amount of power available for a given area. In existing wind farms, wakes can lead to power losses of up to 40% [3]. Inducing early tip vortex breakdown could help mitigate these detrimental wake effects by enhancing mixing between wake and free-stream and by reducing the amount of coherent vortical structures in the flow.

Tip vortices are subject to various instabilities due to their helical geometry, which can cause them to break down. Since the work of Widnall [4] and Gupta & Loewy [5], it is known that helical vortex systems are inherently unstable. Certain types of deformations are naturally amplified by a mechanism of pairing between successive loops of the helical vortices. These instabilities have been identified as one of the first steps in the deconstruction of the wake of a rotor and its return to equilibrium with the external flow. The instabilities fall into two categories: short-wave and long-wave instabilities [6]. Short-wave instabilities are characterized by perturbations within the vortex core, whereas long-wave instabilities involve displacement of the entire vortex. Long-wave instabilities, which are the focus of the current investigation, lead to pairing between adjacent vortex loops and leapfrogging, where the upstream loop rolls up around and passes in front of the downstream loop. This pairing has been shown to play a significant role in tip vortex breakdown [1, 7].

Recent laboratory experiments and numerical simulations by the authors have shown that tip vortex instabilities can be excited, and hereby accelerate their destruction, by adding particular disturbances (Sarmast et al. [8], Sørensen et al. [9], Quaranta et al. [10], Ramos-García et al. [11], Abraham & Leweke [12]). Among these unstable disturbances are those that can be generated by an asymmetry of the rotor. An intentional asymmetry can be created on the rotors of wind turbines, and in particular those of the first row facing the wind in a wind farm, in order to accelerate the development of the natural instabilities of the vortex system of the wake. This asymmetry may be in the form of an extension or a different pitch setting of one of the blades, or the addition of a flap at the end of a blade, or different flaps on each of the three blades. These devices can be passive or active, oscillating at a suitably chosen frequency to excite the unstable deformations of the vortices.

This work focuses on simulating configurations of a symmetric and an asymmetric rotor by means of high-fidelity numerical simulations. A computational fluid dynamics (CFD) lattice-Boltzmann method (LBM) [13] code is used to perform blade-resolved and actuator line [14] simulations of a rotor,

which are validated with experimental data. The LBM has been successfully coupled with the actuator line method by various groups to simulate wind turbines [15, 16, 17, 18] and tidal turbines [19, 20]. Blade-resolved simulations are expected to be very accurate, but unfeasible for simulation of full wind farms, which is where the less costly actuator line simulations can contribute, as they are typically orders of magnitude faster than blade-resolved simulations. Both methods are validated with experiments, with an emphasis on highlighting the limitations of the actuator line method for our test case.

2. Experimental Setup and Flow Conditions

The experiments used for model validation in the current study were conducted in a recirculating free-surface water channel with a test section of dimensions 150 cm $\times$ 38 cm $\times$ 50 cm. A three-bladed rotor was mounted on a shaft with a 1.5 cm diameter, which extends 96 cm downstream to a gearbox connecting the shaft to a stepper motor outside of the water. The rotor has a radius of $R = 9$ cm and the blade cross-sections are NACA2414 airfoils. The tip chord is $c_{tip} = 2.3$ cm, yielding a tip chord-based Reynolds number of $Re = 2\pi f R c_{tip}/\nu \approx 40,000$, where $f = 3$ Hz is the rotation frequency and ν is the fluid kinematic viscosity. Each blade can be detached from the hub individually, enabling the replacement of one or two blades with a slightly modified version to introduce rotor asymmetry. A sketch of the experiment is shown in Fig. 1. The chord c and twist θ distributions of the rotor blade over the radius r are shown in Fig. 2.

The rotor was operated at a tip speed ratio of $\lambda = 2\pi f R/U_\infty = \Omega R/U_\infty = 3$, with a free-stream flow speed of $U_\infty = 56$ cm/s and where Ω is the rotor angular velocity. Blade deformation was not deemed substantial and all simulations in this work assume undeformed blades. To visualize the helical tip vortices, fluorescent dye was applied to the blade tips before the rotor was lowered into the water. Once the rotor was submerged and spinning, LED panels were used to illuminate the test section, causing the dye entrained in the tip vortices to fluoresce. Particle image velocimetry was also conducted at two resolutions, 0.88 mm and 0.16 mm, to capture the whole wake and tip vortex velocity fields, respectively. Additional details about the experiment are provided in [12] and the rotor geometry is provided as a supplement to this work.

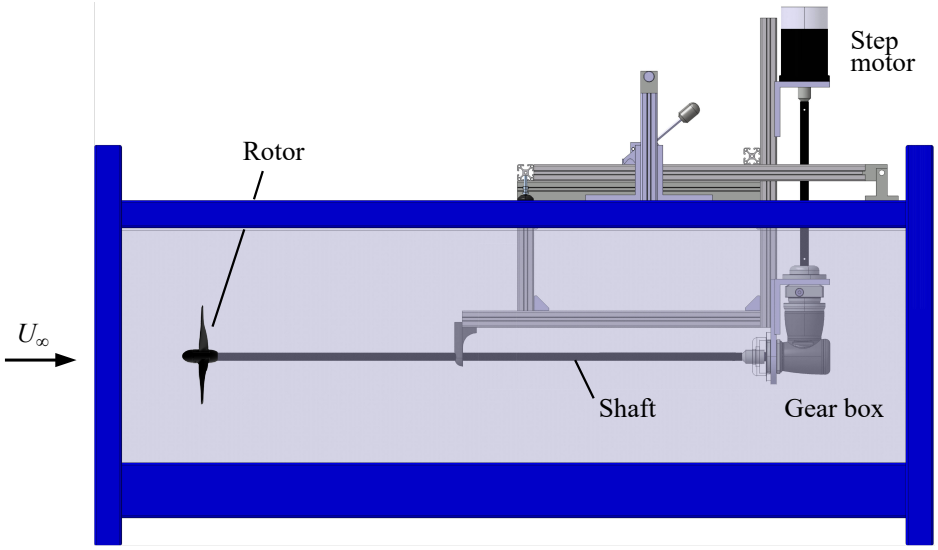

Figure 1: Experimental setup.

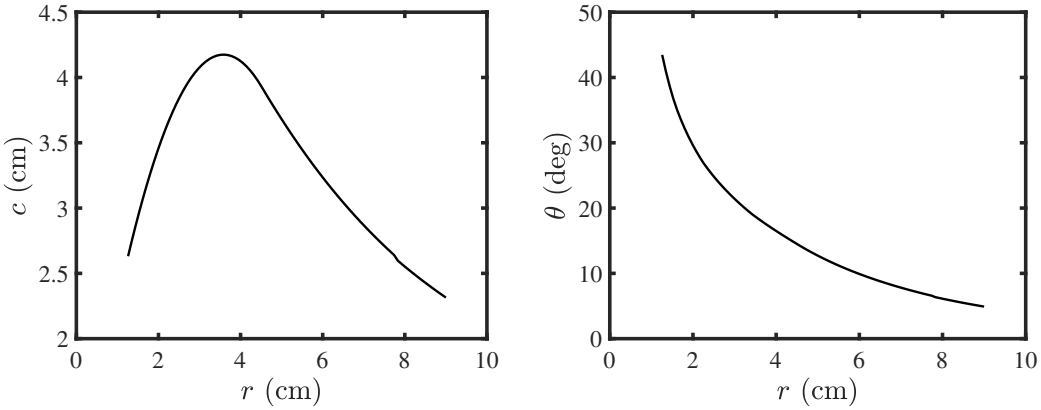

(a) Chord distribution

(b) Twist distribution

Figure 2: Description of the blade geometry.

3. Numerical Methods

3.1. The Lattice-Boltzmann Method

In the last two decades, the LBM [13] has been growing in popularity as an alternative to traditional Navier-Stokes solvers. The objective is the same: to have a description of the velocity and pressure fields over time, based on a certain mesh and time steps. However, instead of using continuum

mechanics as the foundation for describing fluid flow, statistical mechanics are used, considering the fluid as particles that interact with each other and the boundary conditions. A thorough description of the LBM can be found in [21]. Using the Chapman-Enskog expansion [22], the Euler and Navier-Stokes equations can be obtained from the LBM [23].

We first need to consider that a particle can be in a certain spatial coordinate $\vec{x}$. Then, we consider that the particle has a certain velocity $\vec{c}$. These quantities change as a function of time t. As dealing with individual particles quickly becomes too expensive, we instead work with the distribution function $f(\vec{x}, \vec{c}, t)$, which represents the probability that particles at position $\vec{x}$ and time t have the velocity $\vec{c}$. This can also be interpreted as the number of particles in a certain location and time that are travelling with a certain velocity. Fluid properties can be extracted from the moments of the distribution function. The distribution of f is governed by the Boltzmann equation:

$$\frac{d}{dt} f(\vec{x}, \vec{c}, t) = \frac{\partial}{\partial t} f(\vec{x}, \vec{c}, t) + \vec{c} \nabla f(\vec{x}, \vec{c}, t) = C \tag{1}$$

where C is the collision operator, which defines how particles interact. As the Navier-Stokes equations, this can be discretized in time and space, but additionally, the velocity space must also be finite, so that the Boltzmann equation can be solved numerically. These assumptions lead to the Lattice-Boltzmann equation, which, including a body force F, takes the form:

$$f_i(\vec{x} + \vec{c}_i \Delta t, t + \Delta t) = f_i(\vec{x}, t) + C_i(\vec{x}, t) + \Delta t F_i(\vec{x}, t) \tag{2}$$

where the subscript i denotes one of the velocity components that particles are assumed to be able to travel in and Δt is the timestep. As in the Navier-Stokes equations, body forces are added in order to simulate the effect of gravity, Coriolis forces, or other fields that affect the flow. Equation 2 can be interpreted as such: the particle density function for discrete $\vec{x}$, $\vec{c}$, t is computed based on two processes, the advection and the collision steps. In the advection step, a particle is streamed from one cell to another by $\vec{c}\Delta t$. One key factor of this step is that no interpolation is needed to compute fluxes, as in the advection of the Navier-Stokes equations. This makes this step very inexpensive, computationally, while also making it have little numerical dissipation. The physical duration of a timestep in isothermal LBM is given by:

$$\Delta t = \frac{\Delta}{\sqrt{3}c_0} \tag{3}$$

where Δ is the mesh size and c_0 is the speed of sound. Therefore, decreasing the speed of sound allows the simulations to be conducted at larger physical timesteps, which is advantageous for performance and can be done as long as compressibility effects are not important.

The collision step accounts for the interaction between particles with different velocities in the same cell. This is usually computed with the Bhatnagar-Gross-Krook (BGK) model [24], given by:

$$C_i(\vec{x}, t) = -\frac{1}{\tau}\left[f_i(\vec{x}, t) - f_i^{eq}(\vec{x}, t)\right] \tag{4}$$

where τ is the relaxation time and f_i^{eq} is the equilibrium particle distribution function. We can compute τ based on the kinematic viscosity ν, the speed of sound, and Δt as:

$$\tau = \frac{\nu}{c_0^2} + \frac{\Delta t}{2} \tag{5}$$

and f_i^{eq} is:

$$f_i^{eq} = \rho w_i e^{\vec{c}_i \cdot \vec{u}/T - \vec{u}\cdot\vec{u}/(2T)} \tag{6}$$

where ρ is the fluid density, w_i are the weighting factors for each velocity direction, and T is the temperature. We can approximate f_i^{eq} by a third order expansion [25] as:

$$f_i^{eq} \approx \rho w_i \left[1 + \frac{\vec{c}_i \cdot \vec{u}}{T} + \frac{1}{2}\left(\frac{\vec{c}_i \cdot \vec{u}}{T}\right)^2 + \frac{1}{6}\left(\frac{\vec{c}_i \cdot \vec{u}}{T}\right)^3 - \frac{\vec{u}\cdot\vec{u}}{2T}\left(1 + \frac{\vec{c}_i \cdot \vec{u}}{T}\right)\right] \tag{7}$$

Finally, with f_i computed, the fluid density and momentum can be calculated by:

$$\rho = \sum f_i \tag{8}$$

$$\rho\vec{u} = \sum \vec{c}_i f_i \tag{9}$$

And pressure can be computed from the ideal gas law:

$$p = \rho RT \tag{10}$$

where R is the specific gas constant. Note that pressure is not needed during the computations and is calculated only as a post-processing step. This is advantageous when working with compressible air flow, where the large number of digits in the fluid pressure often require double precision in numerical computations.

Advantages of the LBM over traditional Navier-Stokes simulations are mostly related to the simple and computationally inexpensive mathematics of the method. Collision operators are fully local, which is highly advantageous for simulations using large computer clusters and GPUs. The advection step does require neighbor information, but only adjacent cells are used, while the low dissipation in the method is similar to high-order traditional schemes [26], which require several neighbors of given cells. With these advantages, the LBM can be orders of magnitude faster than high-fidelity Navier-Stokes solvers, while the explicit time marching scheme allows for the capturing of high-frequency flow phenomena [27]. Additionally, the Cartesian meshes typically associated with the LBM allow for very complex geometries to be included in simulations [28] with little user effort.

3.2. Flow Solver Specifics

In this work, the commercial LBM code PowerFLOW® is used. This tool has been used extensively for aerodynamics of attached and separated flows [29, 30, 31, 32] rotor aerodynamics [33, 34, 35, 36, 37], and vortical flows [38, 39]. Turbulence modelling is achieved with a $k - \epsilon$ RNG model [40], with the eddy viscosity being reduced depending on local flow properties [41], which is referred to as very large eddy simulation (VLES). The eddy viscosity is added to the fluid viscosity in the BGK model [41], analogous to what is done in Navier-Stokes turbulence modelling with the Boussinesq approximation. This is done by replacing the relaxation time τ in Eq. 4 with an effective relaxation time τ_{eff} [42]:

$$\tau_{\text{eff}} = \tau + C_\mu \frac{k^2/\epsilon}{T\sqrt{(1+\tilde{\eta}^2)}} \tag{11}$$

where C_μ is a constant of the turbulence model, k is the turbulence kinetic energy, ϵ is the turbulence dissipation rate, and $\tilde{\eta}$ is a proprietary combination of local strain and local vorticity. Hence, VLES works by reducing the

eddy viscosity in the presence of resolved turbulence, switching from a $k-\epsilon$ RNG formulation to a large eddy simulation approach based on local flow properties.

The choice of the discretization of the velocity space is a critical part of the LBM. In general, the fewer directions particles can travel into, the less physics are captured by the method. However, the more directions, the higher the computational cost. For isothermal, quasi-incompressible cases, particles only need to travel to adjacent cells for mass and momentum conservation to be achieved. A cost-effective option is to use the D3Q19 formulation, i.e., a 3D 19-states model. This means that particles can travel to 18 adjacent cells, or stay in their current cell (stop state). This is shown in Fig. 3, where the circles denote the directions particles can travel in, for a lattice of cubic cells. With this formulation, the weights ω_i become 1/3 for the stop state, 1/12 for the Cartesian directions, and 1/36 for the diagonals.

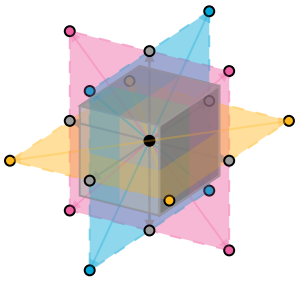

Figure 3: Discretization of the velocity space into 19 vectors.

Body forces are generally simple to apply in Navier-Stokes solvers, but LBM requires some corrections. In PowerFLOW, the formulation of Guo et al. [43] is used, where the body force components F_i in Eq. 2 are computed from a general body force per cell volume $\vec{F}$ using:

$$F_i = \left(1 - \frac{1}{2\tau}\right) \omega_i \left(\frac{\vec{c_i} - \vec{u}}{c_0^2} + \frac{\vec{c_i} \cdot \vec{u}}{c_0^4} \vec{c_i}\right) \cdot \vec{F} \tag{12}$$

This formulation also requires a correction to Eq. 9:

$$\rho \vec{u} = \sum \vec{c_i} f_i + \frac{\Delta t}{2} \vec{F} \tag{13}$$

At solid walls, LBM traditionally has two simple boundary conditions: specular reflection and bounce-back. Specular reflection is equivalent to a

free-slip boundary condition, where the wall tangential component of the particles are preserved, whereas bounce-back is equivalent to no-slip, with the tangential components being reflected back. For both cases, particle components normal to the wall are reflected back into the cells. The normal momentum exchange between particles and solids corresponds to pressure, while the tangential exchange corresponds to friction. This means velocity gradients do not need to be computed in LBM for friction calculation.

A combination of specular reflection and bounce-back can be used to achieve a fluid velocity near the wall that is larger than zero, but smaller than the equivalent inviscid velocity. This is needed for the use of wall models, which are typically needed for Cartesian grids. PowerFLOW uses the log-law as a wall model [44]. Let us define $u_+ = u/u_\tau$ and $y_+ = yu_\tau/\rho$, where u_+ is a non-dimensional velocity, u is the wall tangential velocity, $u_\tau = \sqrt{\tau/\rho}$ is the friction velocity, τ is the shear stress, y_+ is the non-dimensional wall distance, and y is the wall-normal distance, usually measured half a cell from the wall. Hence, the velocity can be computed for the sub-laminar and turbulent regions as:

$$u_+ = \begin{cases} y_+, & \text{if } y_+ < 5 \\ \frac{1}{\kappa} ln(y_+) + C, & \text{if } y_+ > 35 \end{cases}$$

where $\kappa \approx 0.41$ is the von Kármán constant and C is an empirical constant, typically equal to 5.5, but here also includes proprietary pressure gradient corrections. Between these well defined regions, where $5 < y_+ < 35$, u_+ is not well defined and different codes use different methods. In PowerFLOW, an additional logarithmic equation is fitted between the sub-laminar and turbulent regions. The wall treatment has been recently improved to capture resolved turbulence in sufficiently resolved boundary layers, which allows for laminar separation bubbles to be captured [45, 46].

For velocity inlet and pressure outlet boundary conditions, the formulation of Zou and He [47] is used. This formulation is used to define f_i that point from the inlet and outlet faces into the fluid domain. This is achieved by imposing a certain velocity or density (derived from a user-imposed pressure by using the ideal gas law) at the cells adjacent to the boundaries in Eqs. 8 or 9, respectively. Then, we assume that the non-equilibrium part of the particle distributions (the term in square brackets in Eq. 4) performs a bounce-back at the boundaries. This gives us a closed system of equations, allowing the values of f_i entering the domain to be computed.

All the boundary conditions described so far assume the domain boundaries are flat surfaces adjacent to cell faces. For complex geometries, PowerFLOW uses surface elements with second order accuracy, dubbed surfels [48]. Surfels are flat elements generated by the intersection between the fluid mesh and surface facets. Figure 4 shows a 2D representation of how surfels are formed. Note that some cells have more than one surfel. During the discretization of the domain, surfels and their associated Pgrams (simple parallelograms in 2D) are created. The Pgrams define which cells interact with a given surfel, both sending and receiving particles to and from that surfel. They are formed by extruding the surfel along the velocity space directions i.

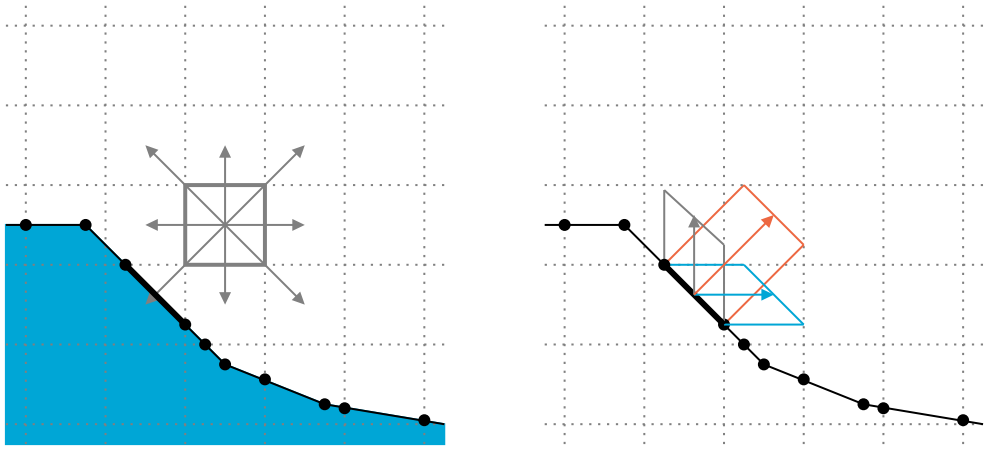

(a) Solid geometry (blue) with a highlighted surfel (bold black line) interacting with the highlighted cell (bold grey box).

(b) Pgrams associated with the highlighted surfel. Grey and blue Pgrams interact with two cells each, orange Pgram interacts with four cells.

Figure 4: Two-dimensional representation of surfels (black lines split by black circles) and their interaction with the particle velocity space (grey arrows) of a lattice (dotted grey lines).

The computations start with the gathering step, where the volume fraction of each cell covered by Pgram i defines the fraction of f_{i*} that will interact with the surfel, where $*$ denotes the direction opposite of the Pgram extrusion. In Fig. 4, that means that for the orange Pgram, around 60% of f_i traveling towards the bottom left diagonal of the grey cell is advected to the highlighted surfel, and 40% of the same f_i is advected to the cell where the surfel is. The second step is surfel collision, where all the particles that reach the surfel interact and the outgoing values of f_i become:

$$f_i = f_i^{eq} + \left(1 - \frac{1}{\tau}\right)(f_{i*} - f_{i*}^{eq}) \tag{14}$$

where again $*$ denotes the incoming particle distribution functions, τ is computed with Eq. 5 with $\nu = 0$, effectively making this a specular reflection (which will be corrected), and f_i^{eq} is computed with Eq. 7, by using the Pgram weighted volume averaged surfel density and tangential velocity as ρ and $\vec{u}$ respectively. Finally, the scattering step is performed, with the particles being redistributed to nearby cells based on the fraction of the volume of the Pgram that they occupy. This step needs a few corrections. The first is a mass flux correction, to ensure the method is conservative and the number of particles coming in match the number of particles coming out. Then, a friction correction can be added to avoid a full specular reflection, allowing for wall functions to be used. Finally, a velocity gradient correction is added to make the scheme second order, avoiding the first order piece-wise constant assumption of the method described so far. The method is thus conservative and lacks the lattice alignment issues of first order methods. A thorough explanation of surfels and all the corrections is provided in the thesis of Li [49].

For rotations, PowerFLOW uses a sliding mesh approach [50]. This is achieved by rotating the geometry inside an axisymmetric region of the mesh, which is separated from the inertial domain by an interface made of surfels. Inside the sliding mesh, effects of inertial forces due to rotations are accounted for by a second order method, using Eq. 12. The velocities in the sliding mesh are shifted based on Eq. 13.

At the interface between the rotating (internal) and inertial (external or fixed) domains, surfels are used on both sides. They coincide in the first time step and, after that, one external surfel will overlap with one or two internal surfels. This is shown in Fig. 5. The way particles are advected across the sliding mesh interface is very similar to the wall treatment described in the previous paragraphs. The gathering step is performed on all surfels, both internal and external. Then a modified surfel collision step is done, but here Eq. 7 uses the velocity vector and not the tangential velocity vector, preserving the momentum normal to the interface. In the internal domain, the velocity is computed in the rotating reference frame. The information that needs to cross the interface is interpolated by a projected area weight ξ. This is also shown in Fig. 5, where the particles from the top external surfel are split between the two surfels that overlap with it using ξ on the left side

and $1 - \xi$ on the right, which is conservative. Finally, the streaming step is performed in the internal and external domains.

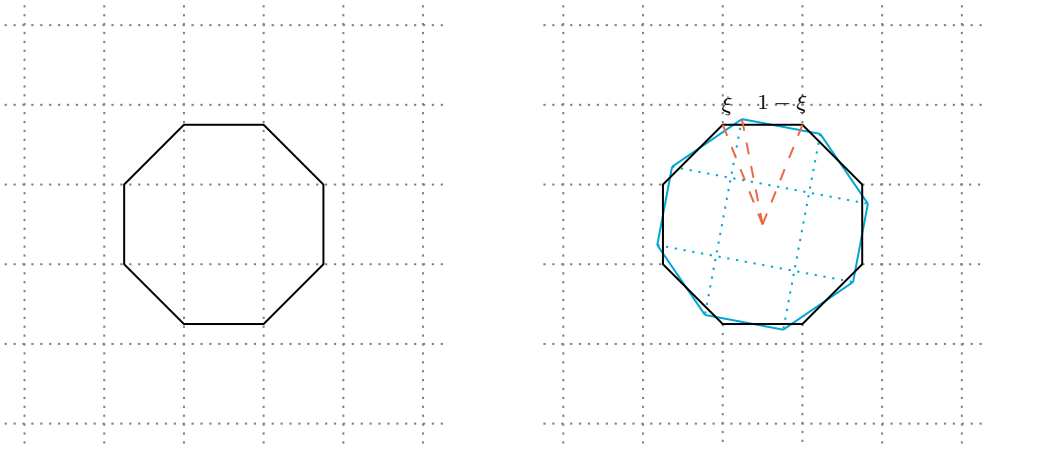

(a) Starting position

(b) Rotated position (rotating reference frame in blue), with the dashed orange lines representing how the particles that reach the top surfel of the external mesh are split between the two internal mesh surfels that overlap with it

Figure 5: Sliding mesh approach, with the background lattice (dotted grey lines) and reference frame interface surfels (solid lines).

3.3. Actuator Line

The actuator line (AL) method [14] was created to allow for high-fidelity simulations of rotors with reduced cost. This is achieved by replacing the blades with body forces in a CFD simulation, allowing for much coarser meshes to be used. AL was recently implemented in the LBM software PowerFLOW [18] using a sliding mesh. This method is referred to as AL-LBM.

A sketch of the vectors involved in blade element theory is shown in Fig. 6. The relative flow velocity ($\vec{U}_r$) is sampled on points along the fictitious blade in the CFD simulation using trilinear interpolation, based on the axial ($\vec{U}_a$) and tangential ($\vec{U}_t$) velocities in the reference frame of the blade, the latter including blade rotation. With the known blade twist (θ), the angle of attack (α) can be computed and 2D airfoil data is then used to compute the local lift ($\vec{L}$) and drag ($\vec{D}$) forces. These forces can then be projected on the axial ($\vec{F}_a$) and tangential ($\vec{F}_t$) directions and imposed as body forces in the CFD simulation.

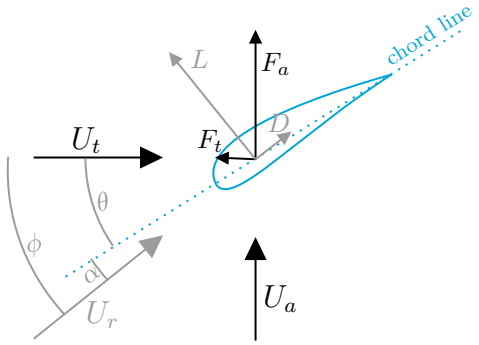

Figure 6: Vectors and angles involved in 2D flow around the cross-section of a rotor blade.

In order to impose a smooth force distribution, smearing functions are used, distributing the original 2D airfoil force $\vec{F}_{2D}$ acting on the airfoil quarter-chord $\vec{x}_0$ into the CFD simulation as $\vec{F}_{CFD}(\vec{x})$, where $\vec{x}$ is the spatial position. The most common smearing function used in AL is a Gaussian with a single smearing factor ϵ, as per Eq. 15.

$$\vec{F}_{CFD}(\vec{x}) = -\vec{F}_{2D}\frac{1}{\epsilon^3\pi^{3/2}}e^{-\frac{\|\vec{x}-\vec{x}_0\|^2}{\epsilon^2}} \tag{15}$$

3.4. Tip Corrections

AL simulations without any special tip treatments tend to have non-physical force distributions near blade tips. Because of this, tip corrections used in blade element momentum theory are often employed in AL, even if these tip corrections were originally designed to compensate for the infinite-number-of-blades assumption in the momentum theory, which is not an assumption of the AL method. A common tip correction is the Glauert one [51], where G, a function of the radial position r, normalized as $\chi = r/R$, and the flow angle ϕ, is defined as:

$$G = \frac{2}{\pi}cos^{-1}\left(e^{-\frac{B(1-\chi)}{2\chi\sin(\phi)}}\right) \tag{16}$$

where B is the number of blades. The root region can use the same correction (replacing $(R-r)$ with $(r-\delta)$, where δ is the radius where the blade lifting surface starts), but alternative formulations for the root correction g have also been proposed [52]:

$$g = 1 - e^{-a(\chi R/\delta)^b} \tag{17}$$

where a and b are empirical constants. Using these methods, G and g are multiplied by the forces along the blades, giving the force distributions a more physical behavior.

A more physically meaningful justification for the issues near blade tips in AL is related to the smearing factor [53]. This smearing of the forces causes the trailing vortices from the blades to effectively have a core, instead of following the inviscid behavior of idealized vortices. This causes the induction on nearby blade sections to be reduced, leading to inaccuracies, in particular near the blade tips. In recent years, smearing corrections derived from attempting to make AL into a method consistent with lifting line were achieved. In this work, AL simulations are performed using the smearing correction of Meyer Forsting et al. [54], instead of Eqs. 16 and 17. This correction compensates for the smearing of the forces from the vortices produced by the actuator line by combining a near-wake model of the trailed vorticity with the Lamb–Oseen viscous core model and coupling it with the AL model.

4. Case Setup

Simulations are conducted in a domain representing the water tunnel used in the experiments. This allows for potential blockage or wall proximity effects to be accounted for. However, the boundary layer on the tunnel walls is assumed to be small and is neglected, by means of free-slip walls in the simulations. A velocity boundary condition is used on the upstream face of the simulation domain and a pressure boundary condition is used on the downstream face, both with constant values in space and time, meaning freestream turbulence is neglected. The experiments were conducted in a water tunnel at low velocities, meaning the flow is incompressible, and hence, Reynolds number matching is important, while the Mach number is less critical. Hence, we simulate the flow assuming air as the fluid, meaning the ideal gas law is used, with the fluid density of air $\rho = 1.23$ kg/m^3, ambient pressure of one atmosphere, and specific gas constant $R = 287$ J/(kgK). However, the viscosity needs to be modified to match the Reynolds number of the experiments, thus ensuring the same physics are being resolved. Hence, we use a fluid viscosity of $\nu = 2\pi f R c_{tip}/Re = 9.75 \times 10^{-7}$. We then modify the speed of sound so that the freestream Mach number is 0.02, instead of the experimental $3.7{\times}10^{-4}$. This is still well within the incompressible range, while providing a timestep that is over 50 times larger than the experimental

Mach number would provide (see Eq. 3), greatly reducing the simulation cost. Thus, the fluid properties used in the simulation do not correspond to an existing fluid, but ensure Reynolds and Mach numbers that are compatible with reproducing the physics in the experiments.

The blade-resolved simulations are done with the first cell size chosen so that the dimensionless distance of the first cell center to the wall $y^+ < 5$, avoiding the use of wall functions, which is possible with the Cartesian mesh due to the low Reynolds number of this case. The tip vortex region is resolved with cubic cells of side $R/45$. A sliding mesh is placed around the blades at a distance of $R/9$. The shaft and hub are included in both the blade-resolved and AL simulations. Cases are initialized with free-stream pressure and velocity. All cases are run for 10 full rotor revolutions.

A radial plane showing the volume mesh used in the blade-resolved simulations is shown in Fig. 7. The sliding mesh interface is sketched as the thick black line. Adjacent resolution levels always change cell size by a factor of two. Besides refinement near the blade surface, to achieve the aforementioned y^+ values, the mesh is refined in the wake of the rotor in regions where the tip vortices are expected to be present, i.e. in a cylinder behind the blade roots and in a hollow cone section behind the blade tips. In these regions, the cell size is $R/225$. The baseline mesh for the AL simulations is nearly identical to the one shown in Fig. 7, but without the small refinement regions near the blades and coarsened by a factor of two.

When mean results are presented, simulations are time-averaged over one rotor rotation and spatially averaged over the azimuth, by taking planes every 5° around the circumference of the domain. Instantaneous results are phase-averaged with 20 samples, by taking planes in the blade reference system over one third of a rotation period. These time and phase-averaging approaches are done to achieve the smoothness seen in the experimental results, which were time or phase-averaged over many turbine rotations.

The smearing factor ϵ is a user-defined aspect of AL, with different authors using a wide range of values. Shives and Crawford [55] found the requirements $\epsilon/c \approx 0.25$ and $\epsilon/\Delta > 4$ to be necessary, where c is the airfoil chord and Δ the local mesh size. Churchfield et al. [56] found $\epsilon/D = 0.035$ to be an adequate ratio, where D is the rotor diameter. Dağ & Sørensen [53] tested ϵ/Δ equal to 3 and 5 and found both to be adequate when using a smearing correction. Kleine et al. [57] found that, for non-planar wings, $\epsilon/\Delta = 7$ produced substantially lower errors than $\epsilon/\Delta = 3.5$.

As previously mentioned, the baseline AL simulations have a cell size

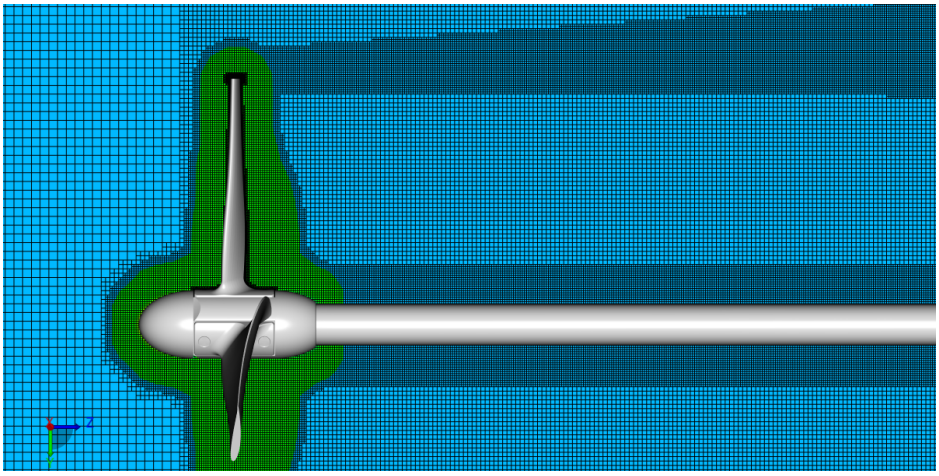

Figure 7: Slice of the mesh used in the blade-resolved simulations. Every second line shown. Blue region shows the inertial reference frame, green region is inside the sliding mesh interface.

around the blades and tip vortex of $\Delta = R/112.5$. We set $\epsilon/\Delta = 7$, meaning for the baseline AL simulations, $\epsilon/c \approx 0.24$ and $\epsilon/D \approx 0.031$. Therefore, based on the recommendations outlined in the previous paragraph, the smearing factor should be adequate for our baseline simulations. In cases where we run a coarse AL simulation, $\Delta = R/56.25$ and in the cases where we match the resolution of the blade-resolved simulations, $\Delta = R/225$. In the latter cases, ϵ is approximately equal to the blade thickness. All AL cases use 43 actuator points along each blade and they all use $\epsilon/\Delta = 7$, regardless of the resolution.

5. Results for the Baseline Rotor

5.1. Validation of Blade-Resolved Simulation

We begin by performing a validation of the blade-resolved simulations. We do this because we will use the axial force along the blades to validate the AL simulations, and these forces are not available in the experiments. Hence, we must first make sure the blade-resolved simulations are capturing the same thrust distribution as the experiments, then we can use these numerical results as a reference. This comparison is done by examining the mean axial velocity $\bar{u}$ in the wake of the rotor, which by momentum theory, is directly related to the thrust distribution.

Figure 8 shows a comparison of $\bar{u}$ along radial (r) lines at several different axial positions (z). The lines are shifted along the horizontal axis for clarity, but the values all start at zero on the bottom of the plots. Excellent agreement between simulations and experiments is achieved for this quantity, giving us confidence that the axial loading on the blades is well captured in the blade-resolved simulations. Further results of the blade-resolved simulations are shown in Section 5.3.

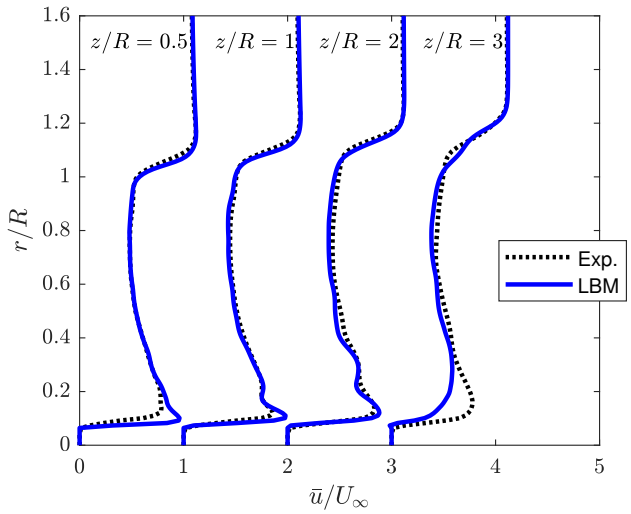

Figure 8: Time and azimuthal-averaged axial velocity at different radial lines. Dotted black lines are experimental data, blue lines are blade-resolved simulations.

5.2. Validation of the Actuator Line Simulations

We now focus on the AL simulations and attempt to match the axial force distribution on the blades from the blade-resolved case. We start by comparing the blade-resolved axial force distribution with AL simulations with different tip mesh resolutions. The AL simulations are performed on a mesh that is two times coarser than the blade-resolved case, which is still quite fine for AL ($\Delta = R/112.5$), and a coarse mesh, coarsened by a factor of two ($\Delta = R/56.25$). Force distributions are shown in Fig. 9 and the thrust coefficients ($C_T = T/(0.5\rho U_\infty^2)$, where T is the integrated thrust) are shown in Table 1. The baseline AL results show substantially less thrust than the reference blade-resolved simulations. As indicated by the coarse mesh results, the thrust slightly improves by coarsening the mesh. This is consistent with

the findings of Nathan et al. [58] and Meyer Forsting and Troldborg [59], who demonstrated that as the grid resolution increases, AL tends to produce lower torque for the same ϵ/Δ. In order to increase the forces acting on the blades, either the mesh needs to be coarsened or ϵ needs to be larger. Neither of these options is adequate for our purposes, as both would lead to thicker tip vortices.

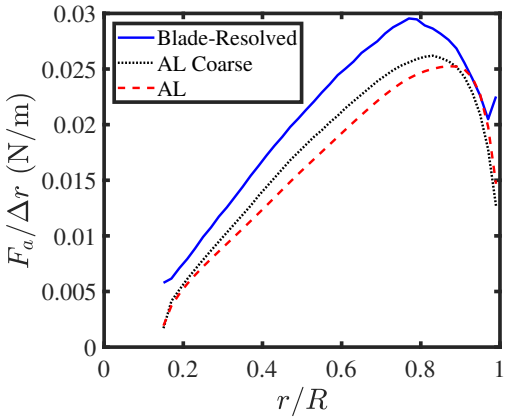

Figure 9: Axial forces along the blades. Blade-resolved simulations compared to different actuator line resolutions.

	C_T	Error
Blade-resolved	0.96	
Actuator line coarse	0.83	14%
Actuator line	0.78	19%

Table 1: Thrust coefficient for each case, along with relative error compared to blade-resolved case.

There are several possible reasons for the discrepancy of AL and blade-resolved simulations. The AL simulations use 2D airfoil data for the NACA2414 airfoil at a Reynolds number (Re) of 30,000, which were obtained using XFOIL [60]. This is a popular airfoil for scaled models, as it is known for having good aerodynamic behavior at low Re. However, this behavior was originally studied for Re starting at $60,000$ [61] and the tip Re for this turbine is $40,000$, which leads to large flow separations according to XFOIL. The very low Re encountered throughout the blade radius led to massive separations in the blade-resolved simulations. Hence, some inaccuracies are

to be expected from the use of the airfoil data. Besides this, the AL technique is based on a blade-element approach, which essentially only is valid for large aspect ratio rotors. In the present case, the aspect ratio is less that four, which is much smaller than what is employed for the conventional wind turbine rotors, where the AL method traditionally has been employed. Corrections for low aspect-ratio blades have been proposed [62], but are not used here.

Figure 10 shows instantaneous surface streamlines from the blade-resolved simulation, demonstrating the 3D flow features. On the pressure side, there is some curvature towards the blade root or tip throughout most of the blade, while on the suction side a large flow separation is present and the streamlines are mostly pointing towards the tip. The images are colored by the pressure coefficient $Cp = (p - p_\infty)/q_\infty$, where p is the static pressure, q the dynamic pressure, and ∞ denotes a free-stream quantity. This massively separated flow makes the AL simulations unreliable for two reasons: first, obtaining polars for separated flows is difficult and depends on Re, meaning highly accurate data would be needed for many angles of attack and Re to represent the entire blade properly. Second, blade element theory, which AL relies on, assumes that the flow around the blades is locally 2D.

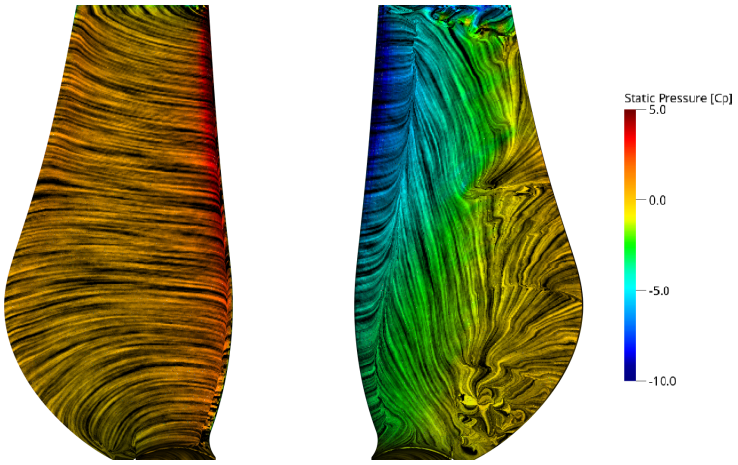

(a) Pressure side (b) Suction side

Figure 10: Line integral convolution showing instantaneous surface streamlines colored by pressure coefficient on a blade.

The issues highlighted in this section put into question the capabilities of AL for our test case and we investigate the potential for AL accuracy further

in the next section.

5.3. Preset Actuator Line Simulations

As discussed in the previous section, AL has limitations linked to low aspect ratio rotors and separated flows. Additionally, likely because of the velocity sampling in the simulation, results can be sensitive to the mesh and the smearing factor sizes [55]. In this section, we verify what the best possible result out of an AL simulation can be for our test case in order to remove the limitations highlighted in the previous section.

Hence, we employ what we refer to as "preset AL". The blades are still modelled as lines composed of Gaussian blobs applying body forces to the CFD simulations. We use the same mesh as the blade-resolved simulations and $\epsilon = 2.8$ mm, which is roughly equal to the blade thickness. However, instead of computing the forces based on sampling the local velocity and using blade element theory, we simply extract the forces on the blades of a blade-resolved simulation and apply them on the preset AL case, with no feedback or table look-ups. No tip or smearing corrections are needed, removing another source of uncertainty. With this method, no assumption of attached 2D flow is made and the only simplification of the rotor in the simulation is that the blades are modelled as actuators instead of walls. The forces are extracted from the blade-resolved simulations by integrating the pressure and friction on the blade surface within rings of constant radii, centered on the locations where the AL body forces are applied.

A second preset AL, which we refer to as "analytical preset AL" only employs thrust and power coefficients as input, whereas the force distribution along the blades is obtained from an analytical model [52]. This model assumes a constant circulation Γ along the blade, with normalized form γ:

$$\gamma = \frac{\Gamma}{4\pi R U_\infty} \tag{18}$$

From momentum theory, the thrust coefficient is:

$$C_T = 2a_1\gamma^2 + 4\lambda a_2 \gamma \tag{19}$$

where a_1 and a_2 are defined as:

$$a_1 = \int_0^1 \frac{g^2 G^2}{\chi} d\chi \tag{20}$$

$$a_2 = \int_0^1 gG\chi d\chi \tag{21}$$

where G and g are defined in Eqs. 16 and 17. For g we use $a = 1.256$ and $b = 2$ [63] and for G we assume the tangential induction is negligible, hence $U_t = \Omega r$ and we can compute the sine term in Eq. 16 as:

$$\frac{1}{\sin(\phi)} = \sqrt{1 + \frac{\lambda^2 r^2 U_\infty^2}{R^2 U_a^2}} \tag{22}$$

Solving Eq. 19 for γ we obtain:

$$\gamma = \frac{-4\lambda a_2 + \sqrt{16\lambda^2 a_2^2 + 8a_1 C_T}}{4a_1} \tag{23}$$

The average axial flow velocity at the rotor disk U_a is calculated using momentum theory as:

$$U_a = \frac{U_\infty C_P}{4\lambda a_2 \gamma} \tag{24}$$

where $C_P = Q\Omega/(0.5\rho\pi R^2 U_\infty^3)$ is the power coefficient, with Q as the rotor torque. With an initial value of U_a, one can compute Eq. 16, update the value of γ, recompute Eq. 24, and after a few iterations converge on a value for U_a and γ. Finally, the axial force distribution F_a and tangential force distribution F_t can be computed as:

$$F_a = \frac{\pi R \rho U_\infty^2 gG}{B} \gamma \left(\frac{2\lambda r}{R} + \frac{\gamma R g G}{r} \right) \tag{25}$$

$$F_t = \frac{\pi R \rho U_\infty^2 gG}{B} \left(\frac{C_P}{2\lambda a_2} \right) \tag{26}$$

Hence, F_a is a function of γ, which depends on C_T, and F_t is a function of C_P.

This analytical approach is more general-purpose than the preset AL, as the amount of information required before conducting the simulation is greatly reduced from full force distributions to C_T and C_P. The drawback is that the force distribution along the blade is not fully correct, but as is shown in Fig 11, it is very close to the blade-resolved results.

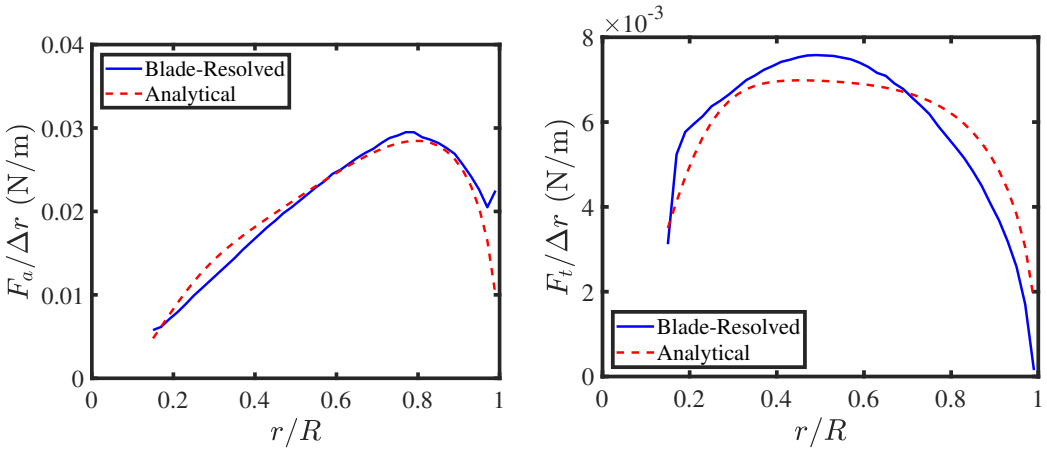

(a) Axial force

(b) Tangential force

Figure 11: Forces along the blades. Blade-resolved simulations compared to analytical model.

Both preset AL approaches used here assume a fixed force on each blade section over time, meaning these approaches are limited to cases where the flow around the blades does not change over time. Hence, in cases with atmospheric boundary layers, rotor yaw, rotor tilt, or freestream turbulence, the use of the preset AL approaches as they are used here would lead to severe accuracy concerns.

The resulting velocity fields are shown in Fig. 12, where we can see the preset AL and blade-resolved results match each other and experimental data very well, with minor difference in the wake of the blade root. The analytical AL results are also in good agreement with the experiments, with differences mostly confined to the wake of the blade root ($r/R < 0.5$). The standard AL results (here using the coarse mesh) show much weaker tip vortices, barely visible using the same color range as the other cases. The lower thrust seen in Fig. 9 is also noticeable here, with the deceleration behind the rotor being less pronounced in the AL case. The blade-resolved case shows a deceleration of the flow near $r/R = 0.1$ and $z/R = 3$ due to the root vortex bursting, which either does not occur in the other case or occurs at a later point. This explains the differences in Fig. 8 near the root of the most downstream line.

Similar results can be seen in Fig. 13, where the radial component of the velocity is shown for each case. The experiments, blade-resolved simulations, and preset AL simulations once again show excellent agreement. The blade-

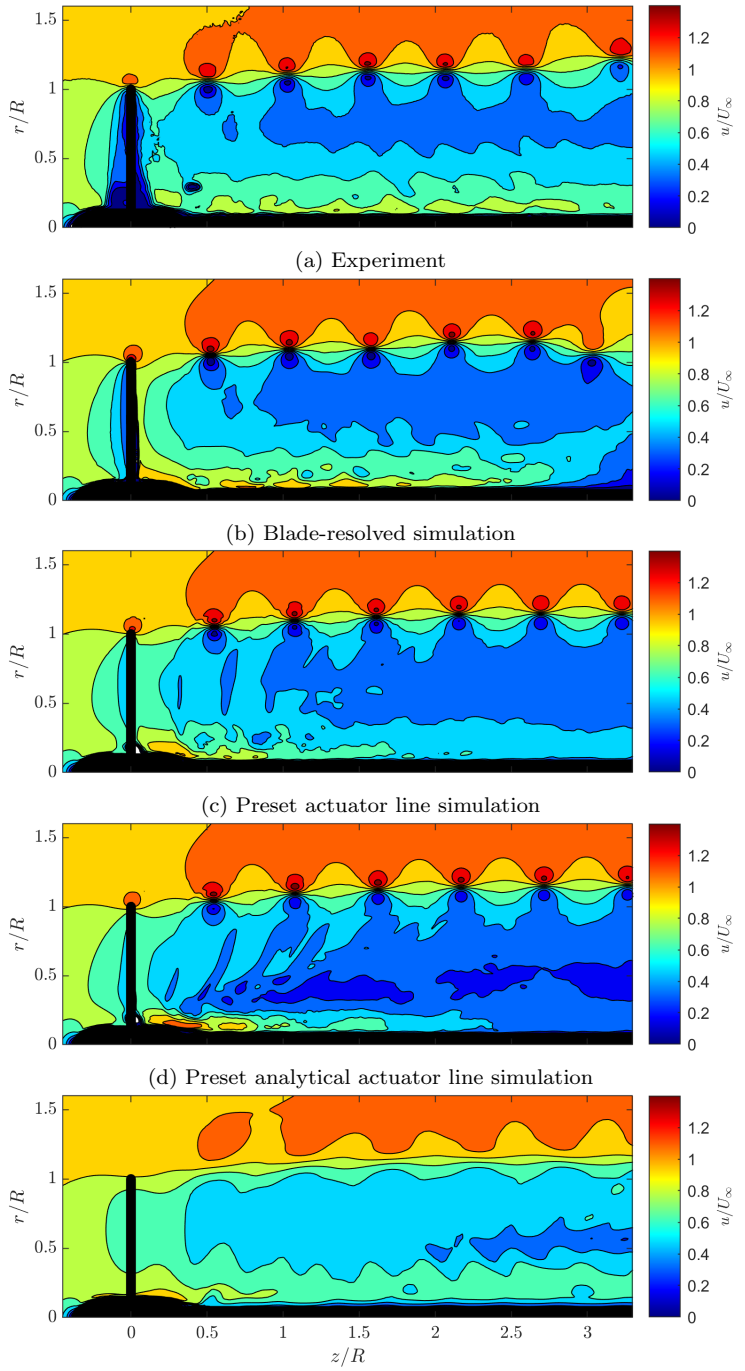

(a) Experiment

(b) Blade-resolved simulation

(c) Preset actuator line simulation

(d) Preset analytical actuator line simulation

(e) Coarse standard actuator line simulation

Figure 12: Phase-averaged axial velocity on a $z-r$ plane.

resolved simulations seems to capture the root vortex more accurately than the preset AL, as evidenced by the contours in $1 < z/R < 2$ and $0 < r/R < 0.5$. The analytical AL results are again very close to the reference cases, with differences mostly in the blade root wake. The coarse AL case clearly has much weaker tip vortices than the other cases.

A notable feature of the experiments and blade-resolved case is that the tip vortex starts becoming misaligned around $z/R = 3$. This is the beginning of the long-wave instability that leads to leapfrogging. For a perfectly symmetric rotor, this should not happen. In the experiments, the presence of very small asymmetries introduced during rotor assembly ($\sim 0.001R$) can lead to these instabilities, while in the simulations the asymmetry due to having a Cartesian mesh (instead of an axisymmetric mesh) could be the main trigger for leapfrogging. Flow separation around the blades and the chaotic nature of the associated turbulence could also be the source of the instabilities. The AL cases, with their very smooth velocity distributions and more simple wake structure do not exhibit any long-wave instabilities.

While the velocity fields for the blade-resolved and preset AL cases look almost identical in the wake of the rotor, the flow around the real blades has strong separations, which lead to some differences. Figure 14 shows the phase-averaged azimuthal velocity, which shows that the wake from the blades is much more visible in the preset AL case. This quantity is not available in the experimental data set. Note the vertical green lines in the blue region of the near wake ($0.2 < z/R < 1.5$). The wakes of the AL blades behave in a steady fashion, while the turbulence in the blade-resolved case causes diffusion, making the wake more difficult to visualize. Overall, using AL leads to higher swirl in the wake.

Finally, we examine the tip vortex itself. Figure 15 shows the phase-averaged rotation velocity v_θ around the tip vortex center, measured in a plane rotated 60° in the azimuthal direction, downstream of one of the blades. We only focus on the experiments, blade-resolved simulations, and preset AL, as the standard AL simulations produced tip vortices that were clearly too weak, as the thrust distributions indicate, and the analytical preset AL results are very similar to the preset AL. Experimental results are available in low resolution (0.88 mm), which is the resolution used in the PIV shown in the previous sections, and high resolution (0.16 mm), where the field of view was reduced to a small area around the tip vortex location. The difference between the two experimental curves indicates how difficult it is to capture the vortex core accurately. The preset AL and blade-resolved simulations

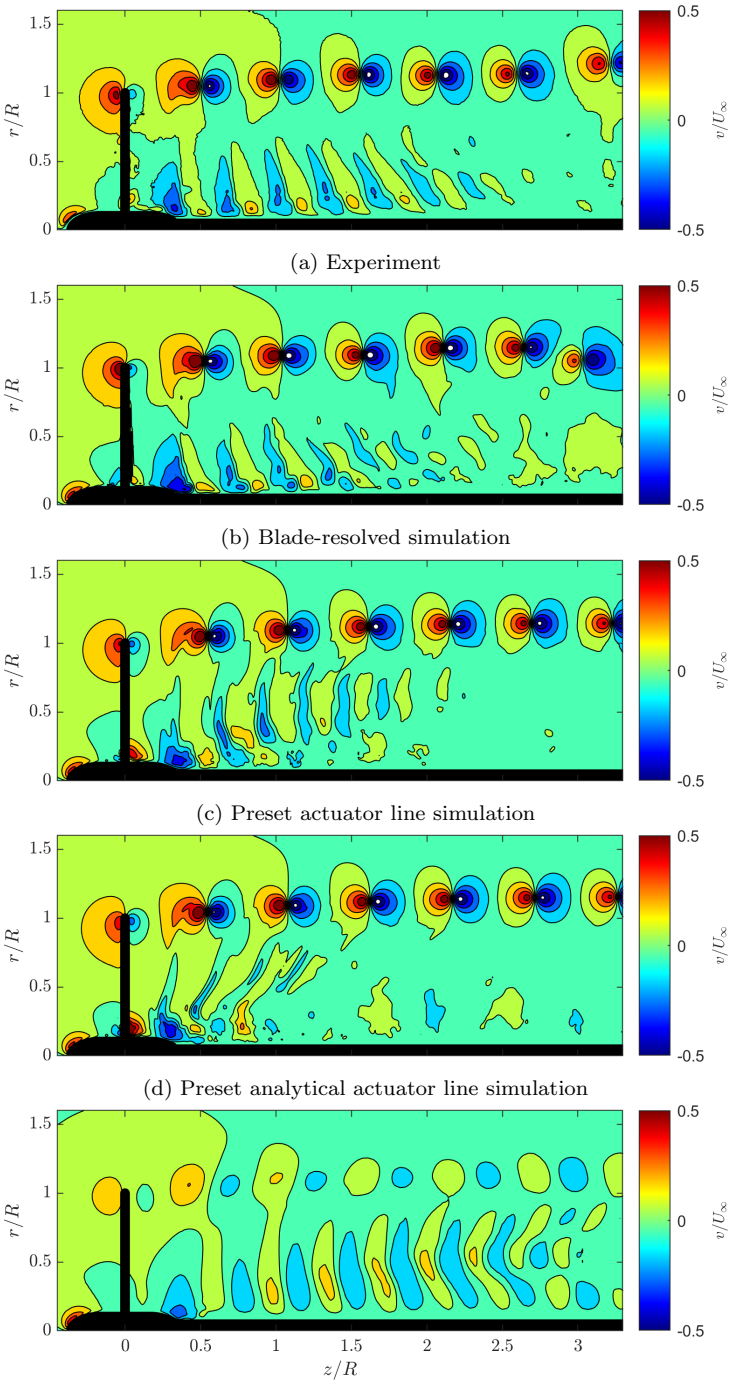

(a) Experiment

(b) Blade-resolved simulation

(c) Preset actuator line simulation

(d) Preset analytical actuator line simulation

(e) Coarse standard actuator line simulation

Figure 13: Phase-averaged radial velocity on a $z-r$ plane.

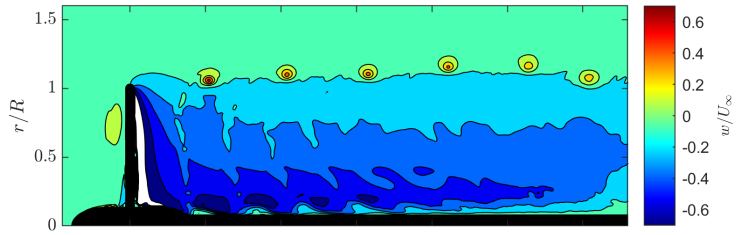

(a) Blade-resolved simulation

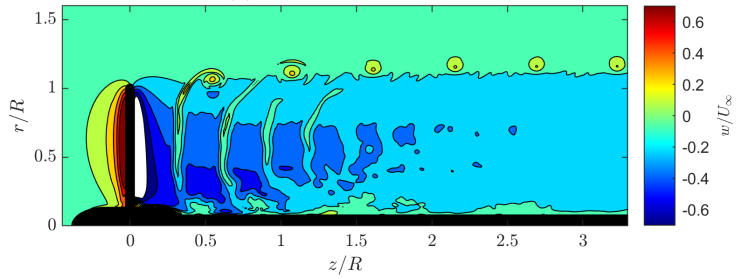

(b) Preset actuator line simulation

Figure 14: Phase-averaged azimuthal velocity on a $z-r$ plane.

agree very well with each other, even in terms of the vortex radius (i.e., the value of r corresponding to the maximum value of v_θ), indicating the choice of ϵ is adequate. Both simulations match the velocities induced by the vortex outside of the laminar core for $r > 8$ mm. This agreement means that the vortex circulation is well captured by the simulations, which is consistent with the axial and radial velocity agreement shown in Figs. 12 and 13. The cell size in the simulations is 0.4 mm, which is too large to capture the core size measured in the experiments (about 1.5 mm). For short-wave instabilities, matching the vortex core is important, whereas for long-wave instabilities, matching the circulation should be enough.

6. Asymmetric Rotor Simulations

6.1. Validation with Experiments

Here, we simulate cases where one of the blades of the rotor is modified, in order to promote wake instability and earlier recovery. We focus on a case from previous work [12]: extending the radius of one blade by 4.1% ($R = 9.37$ cm). The extended blade geometry is provided as a supplement to this work. The helical vortex system from the experiments, blade-resolved simulation, preset AL simulation, and coarse AL simulation are shown in

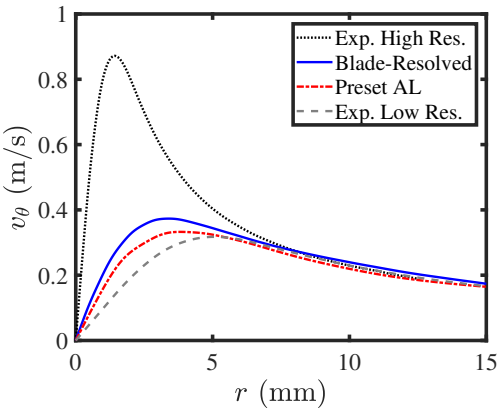

Figure 15: Tangential velocity around the tip vortex core.

Fig. 16. The blade-resolved simulations show strong short-wave instabilities in the tip vortex, while also capturing secondary flow structures around the tip vortex, which begin near the blade, where massive flow separation occurs. These secondary structures, or turbulent worms [64], are not visible in the experiments, which may be due to the dye being entrained only in the primary tip vortex. They have been shown to occur in reality, but are only numerically captured via blade-resolved, scale-resolved simulations [65]. The coarse AL results have a much thicker tip vortex, due to the low resolution and high ϵ. All cases capture the leapfrogging that occurs in the helical wake due to the asymmetric rotor.

The distance z_L from the rotor plane where leapfrogging, or the swapping of axial positions between two adjacent vortex loops, occurs was measured for each case. It is compared to experimental data [12] in Table 2. In both simulation and experiment the leapfrogging location was determined visually as the point where two successive loops have the same axial coordinate. As previously discussed, small imperfections in simulations and experiments lead to leapfrogging in experiments and blade-resolved simulations of the symmetric rotor. The AL simulations are much less turbulent than the blade-resolved ones, with effectively steady flow around the fictitious blades. Hence, in AL leapfrogging does not occur, whereas in blade-resolved simulations and in experiments it occurs at similar locations for reasons that could be coincidental.

When one blade is extended, the asymmetry introduces a disturbance in the helical vortex system that leads to leapfrogging. The blade-resolved

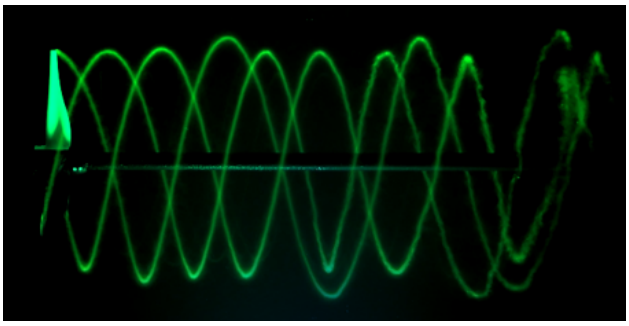

(a) Experimental results, dye visualization [12]

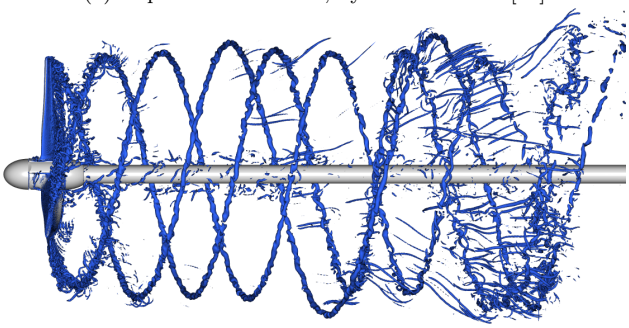

(b) Blade-resolved simulation, isosurface of $\lambda_2 = -300R^2/U_\infty^2$

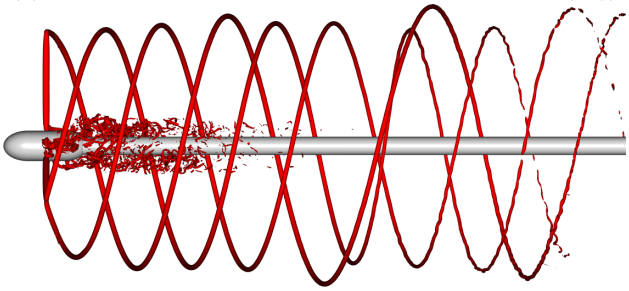

(c) Preset actuator line simulation, isosurface of $\lambda_2 = -300R^2/U_\infty^2$

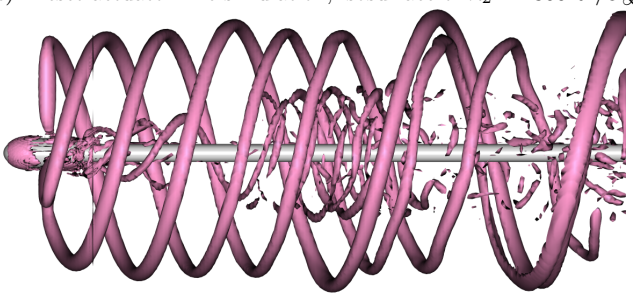

(d) Coarse standard actuator line simulation, isosurface of $\lambda_2 = -5R^2/U_\infty^2$

Figure 16: Visualization of tip vortex for extended blade case.

	Baseline	Extended
Experiment [12]	4.09	2.73
Blade-resolved	4.1	2.9
Preset actuator line	No	3.1
Actuator line	No	3.7

Table 2: Streamwise position z_L/R where leapfrogging occurs for each case.

simulations capture leapfrogging within 6% of experimental values, whereas the AL simulations overshoot the leapfrogging location by 14% for the preset case and 36% for the coarse AL case. The steady nature of the vortex system in AL is likely responsible for stabilizing the helical vortex system. Hence, AL is not suitable for predicting the exact location of tip vortex instability for laminar inflows, but can likely still be used for turbulent inflow and wind farm studies, where the exact instability location is less relevant than the far-wake mixing.

6.2. Far-Wake Analysis

We now go beyond the experiments, which were limited to the near-wake, and move on to simulating the far-wake, in order to investigate the potential wake-recovery benefits of the asymmetric rotor. We extend the simulation domain downstream, in order to examine the wake up to a distance of $14R$ of the rotor. Simulations are conducted with the preset AL method, in order to save computational time, and the shaft is removed. The tip vortices for the baseline and symmetric rotor are shown in Fig. 17. In spite of the smooth vortices of AL, the asymmetric case eventually develops instabilities, near $z/R = 6.5$. This is likely due to small asymmetries in the flow introduced by the Cartesian mesh and potential short-wave instabilities, which are not axisymmetric. The asymmetric rotor still leads to leapfrogging in under half the distance ($z_L/R = 3.1$), meaning it is still likely to lead to better wake recovery.

The power available for a wind turbine is proportional to u^3. This allows us to estimate the available power for wind turbines downstream of our rotor, normalized by the power available to our rotor:

$$\text{Available Power} = \frac{\int u^3 \mathrm{d}A}{\int U_\infty^3 \mathrm{d}A} \tag{27}$$

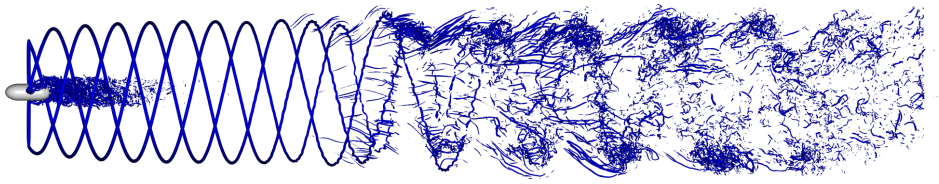

(a) Symmetric rotor

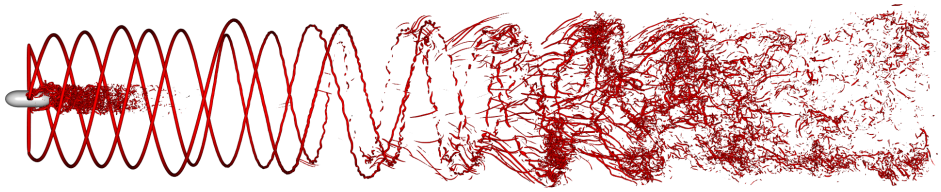

(b) Asymmetric rotor

Figure 17: Visualization of tip vortex for extended domain cases. Preset AL, isosurface of $\lambda_2 = -200R^2/U_\infty^2$.

where A refers to the area of a disk of radius R perpendicular to, and centered on, the rotor axis, at several z/R locations. The results of this analysis are shown in Fig. 18. At a distance of $14R$, the asymmetric rotor allows for 12% more power to reach a potential wind turbine, in spite of the longer blade leading to slightly more thrust than the symmetric rotor. This demonstrates the potential of the tip extension for far-wake recovery in a wind farm.

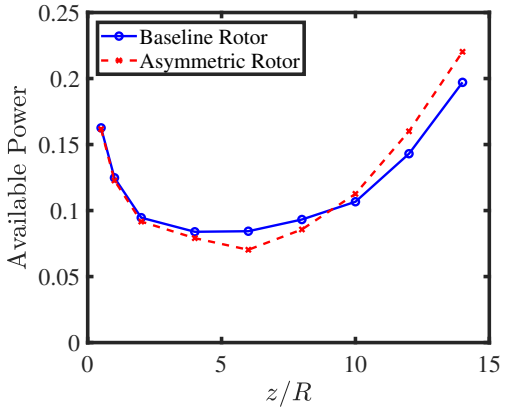

Figure 18: Available power in the wake of the rotor.

7. Conclusions and Outlook

Blade-resolved and actuator line lattice-Boltzmann simulations of a small three-bladed rotor, operating as a wind turbine, were shown in this work. Simulations were validated with experimental data, showing a remarkable agreement for the blade-resolved simulations. The actuator line was shown to have moderate dependence on the mesh resolution. Coarsening the mesh improves the actuator line thrust generation, but also necessarily makes the tip vortices thicker.

Preset actuator line simulations, where the body forces are copied from the blade-resolved simulations, with no feedback from the flow velocity or look-up tables, are conducted. These preset simulations show excellent agreement with blade-resolved simulations and experiments, which leads to the conclusion that it is possible to model this case with actuator line, but the lack of correct airfoil data, and the combination of a 2D blade-element approach with a very low aspect ratio rotor introduce substantial errors. The preset actuator line simulations, using the same tip vortex resolution as the blade-resolved case, used one fifth of the computational resources. It was shown that having the thrust and power of the turbine is sufficient to produce accurate preset actuator line simulations, by using an analytical model to compute the force distributions along the blades.

Tip vortex instability was examined and we found short-wave instabilities in the blade-resolved simulations, which were not visible in the experiments. Long-wave instabilities leading to leapfrogging were found when the rotor was made asymmetric by extending one blade radially. All simulations were able to capture the leapfrogging caused by the asymmetric rotor, with the preset and standard actuator line cases predicting the location of leapfrogging less accurately than the blade-resolved simulations.

Finally, the effects of rotor asymmetry on the far-wake were investigated by using preset actuator line simulations with a longer domain than was available in the experiments. The wake recovery introduced by early leapfrogging led to an increase of 12% in the available power for a downstream turbine perfectly aligned with the rotor, at a distance of 7 rotor diameters.

Future work will focus on simulating different asymmetric rotor configurations, focusing on the effects of vortex instability on wake recovery over long distances. The effect of free-stream turbulence will also be investigated.

References

[1] J. N. Sørensen, Instability of helical tip vortices in rotor wakes, Journal of Fluid Mechanics 682 (2011) 1–4. doi:10.1017/jfm.2011.277.

[2] L. E. M. Lignarolo, D. Ragni, F. Scarano, C. J. Simão Ferreira, G. J. W. Van Bussel, Tip-vortex instability and turbulent mixing in wind-turbine wakes, Journal of Fluid Mechanics 781 (2015) 467–493. doi:10.1017/jfm.2015.470.

[3] J. C. Y. Lee, M. J. Fields, An overview of wind-energy-production prediction bias, losses, and uncertainties, Wind Energy Science 6 (2) (2021) 311–365. doi:10.5194/wes-6-311-2021.

[4] S. E. Widnall, The stability of a helical vortex filament, Journal of Fluid Mechanics 54 (4) (1972) 641–663. doi:10.1017/S0022112072000928.

[5] B. P. Gupta, R. G. Loewy, Theoretical analysis of the aerodynamic stability of multiple, interdigitated helical vortices, AIAA Journal 12 (10) (1974) 1381–1387. doi:10.2514/3.49493.

[6] T. Leweke, H. U. Quaranta, H. Bolnot, F. J. Blanco-Rodríguez, S. L. Dizès, Long- and short-wave instabilities in helical vortices, Journal of Physics: Conference Series 524 (1) (2014) 012154. doi:10.1088/1742-6596/524/1/012154.

[7] M. Felli, R. Camussi, F. Di Felice, Mechanisms of evolution of the propeller wake in the transition and far fields, Journal of Fluid Mechanics 682 (2011) 5–53. doi:10.1017/jfm.2011.150.

[8] S. Sarmast, R. Dadfar, R. F. Mikkelsen, P. Schlatter, S. Ivanell, J. N. Sørensen, D. S. Henningson, Mutual inductance instability of the tip vortices behind a wind turbine, Journal of Fluid Mechanics 755 (2014) 705–731. doi:10.1017/jfm.2014.326.

[9] J. N. Sørensen, R. F. Mikkelsen, D. S. Henningson, S. Ivanell, S. Sarmast, S. J. Andersen, Simulation of wind turbine wakes using the actuator line technique, Philosophical Transactions of the Royal Society A: Mathematical, Physical and Engineering Sciences 373 (2035) (2015) 20140071. doi:10.1098/rsta.2014.0071.

[10] H. U. Quaranta, M. Brynjell-Rahkola, T. Leweke, D. S. Henningson, Local and global pairing instabilities of two interlaced helical vortices, Journal of Fluid Mechanics 863 (2019) 927–955. doi:10.1017/jfm.2018.904.

[11] N. Ramos-García, A. Abraham, T. Leweke, J. N. Sørensen, Multi-fidelity vortex simulations of rotor flows: Validation against detailed wake measurements, Computers & Fluids 255 (2023) 105790. doi:10.1016/j.compfluid.2023.105790.

[12] A. Abraham, T. Leweke, Experimental investigation of blade tip vortex behavior in the wake of asymmetric rotors, Experiments in Fluids 64 (6) (2023) 109. doi:10.1007/s00348-023-03646-3.

[13] H. Chen, C. Teixeira, K. Molvig, Digital physics approach to computational fluid dynamics: Some basic theoretical features, International Journal of Modern Physics C 08 (04) (1997) 675–684. doi:10.1142/S0129183197000576.

[14] J. N. Sørensen, W. Z. Shen, Numerical modeling of wind turbine wakes, Journal of Fluids Engineering 124 (2) (2002) 393–399. doi:10.1115/1.1471361.

[15] S. Rullaud, F. Blondel, M. Cathelain, Actuator-line model in a lattice Boltzmann framework for wind turbine simulations, Journal of Physics: Conference Series 1037 (2018) 022023. doi:10.1088/1742-6596/1037/2/022023.

[16] H. Asmuth, H. Olivares-Espinosa, S. Ivanell, Actuator line simulations of wind turbine wakes using the lattice Boltzmann method, Wind Energy Science 5 (2) (2020) 623–645. doi:10.5194/wes-5-623-2020.

[17] H. Schottenhamml, A. Anciaux-Sedrakian, F. Blondel, A. Borras-Nadal, P.-A. Joulin, U. Rüde, Evaluation of a lattice Boltzmann-based wind-turbine actuator line model against a Navier-Stokes approach, Journal of Physics: Conference Series 2265 (2) (2022) 022027. doi:10.1088/1742-6596/2265/2/022027.

[18] A. F. P. Ribeiro, C. Muscari, Sliding mesh simulations of a wind turbine rotor with actuator line lattice-Boltzmann method, Wind Energy (2023). doi:10.1002/we.2821.

[19] M. Grondeau, S. Guillou, P. Mercier, E. Poizot, Wake of a ducted vertical axis tidal turbine in turbulent flows, LBM actuator-line approach, Energies 12 (22) (2019) 4273. doi:10.3390/en12224273.

[20] S. Watanabe, C. Hu, Lattice Boltzmann simulations for multiple tidal turbines using actuator line model, Journal of Hydrodynamics 34 (3) (2022) 372–381. doi:10.1007/s42241-022-0037-0.

[21] S. Succi, The Lattice Boltzmann Equation: For Fluid Dynamics and Beyond, Clarendon Press, 2001.
URL https://books.google.com/books?id=0C0Sj_xgnhAC

[22] S. Chapman, T. Cowling, D. Burnett, C. Cercignani, The Mathematical Theory of Non-uniform Gases: An Account of the Kinetic Theory of Viscosity, Thermal Conduction and Diffusion in Gases, Cambridge Mathematical Library, Cambridge University Press, 1990.
URL https://books.google.com/books?id=Cbp5JP2OTrwC

[23] H. Chen, S. Chen, W. H. Matthaeus, Recovery of the Navier-Stokes equations using a lattice-gas Boltzmann method, Physical Review A 45 (1992) R5339–R5342. doi:10.1103/PhysRevA.45.R5339.

[24] P. L. Bhatnagar, E. P. Gross, M. Krook, A model for collision processes in gases. I. small amplitude processes in charged and neutral one-component systems, Physical Review 94 (1954) 511–525. doi:10.1103/PhysRev.94.511.

[25] H. Fan, R. Zhang, H. Chen, Extended volumetric scheme for lattice boltzmann models, Physical Review E 73 (2006) 066708. doi:10.1103/PhysRevE.73.066708.

[26] G. Brès, F. Pérot, D. Freed, Properties of the lattice Boltzmann method for acoustics, 15th AIAA/CEAS Aeroacoustics Conference (30th AIAA Aeroacoustics Conference) (2012). doi:10.2514/6.2009-3395.

[27] E. Manoha, B. Caruelle, Summary of the LAGOON solutions from the benchmark problems for airframe noise computations-III workshop, 21st AIAA/CEAS Aeroacoustics Conference (2015). doi:10.2514/6.2015-2846.

[28] M. R. Khorrami, B. Konig, E. Fares, A. Ribeiro, M. Czech, P. A. Ravetta, Airframe noise simulations of a full-scale large civil transport in landing configuration, AIAA AVIATION FORUM (2021). doi:10.2514/6.2021-2161.

[29] A. F. P. Ribeiro, D. Singh, B. Konig, E. Fares, On the stall characteristics of iced wings, 55th AIAA Aerospace Sciences Meeting (2017). doi:10.2514/6.2017-1426.

[30] B. König, D. Singh, A. Ribeiro, E. Fares, Lattice-boltzmann simulations at the corners of the flight envelope, 54th 3AF International Conference on Applied Aerodynamics (2019).

[31] C. L. Rumsey, J. P. Slotnick, A. J. Sclafani, Overview and summary of the third aiaa high lift prediction workshop, Journal of Aircraft 56 (2) (2019) 621–644. doi:10.2514/1.C034940.

[32] B. Konig, B. M. Duda, G. M. Laskowski, Lattice Boltzmann simulations for the 4th AIAA high-lift prediction workshop using PowerFLOW, in: AIAA AVIATION Forum, 2022. doi:10.2514/6.2022-3433.

[33] S. D. Lucas-Bodas, J. Narbona-Gonzalez, V. Ossorio-Contreras, J. Jose, Guerra-Crespo, D. E. Funes-Sebastian, L. P. Ruiz-Calavera, Experimental validation of numerical prediction of wing-propeller aerodynamic interaction, 32nd Congress of the International Council of the Aeronautical Sciences (2021).
URL https://www.icas.org/ICAS_ARCHIVE/ICAS2020/data/papers/ICAS2020_0171_paper.pdf

[34] W. van der Velden, G. Romani, D. Casalino, Validation and insight of a full-scale S-76 helicopter rotor using the lattice-Boltzmann method, Aerospace Science and Technology 118 (2021) 107007. doi:10.1016/j.ast.2021.107007.

[35] D. Casalino, W. C. van der Velden, G. Romani, A framework for multi-fidelity wind-turbine aeroacoustic simulations, 28th AIAA/CEAS Aeroacoustics 2022 Conference (2022). doi:10.2514/6.2022-2892.

[36] G. Romani, E. Grande, F. Avallone, D. Ragni, D. Casalino, Performance and noise prediction of low-Reynolds number propellers using

the lattice-Boltzmann method, Aerospace Science and Technology 125 (2022) 107086, sI: DICUAM 2021. doi:10.1016/j.ast.2021.107086.

[37] A. F. P. Ribeiro, R. Duivenvoorden, D. Martins, High-fidelity simulations of propeller-wing interactions in high-lift conditions, in: AIAA AVIATION Forum, 2023. doi:10.2514/6.2023-3541.

[38] A. F. P. Ribeiro, Unsteady analysis of ground vortex ingestion with LBM-VLES, in: AIAA SCITECH Forum, 2022. doi:10.2514/6.2022-0224.

[39] R. Ferris, M. Sacks, D. Cerizza, A. F. P. Ribeiro, M. R. Khorrami, Aeroacoustic computations of a generic low boom concept in landing configuration: Part 1 - aerodynamic simulations, in: AIAA AVIATION FORUM, 2021. doi:10.2514/6.2021-2195.

[40] V. Yakhot, S. A. Orszag, S. Thangam, T. B. Gatski, C. G. Speziale, Development of turbulence models for shear flows by a double expansion technique, Physics of Fluids A: Fluid Dynamics 4 (7) (1992) 1510–1520. doi:10.1063/1.858424.

[41] E. Fares, B. Duda, A. F. P. Ribeiro, B. König, Scale-resolving simulations using a lattice Boltzmann-based approach, CEAS Aeronautical Journal 9 (4) (2018). doi:10.1007/s13272-018-0317-0.

[42] H. Chen, S. Kandasamy, S. Orszag, R. Shock, S. Succi, V. Yakhot, Extended Boltzmann kinetic equation for turbulent flows, Science 301 (5633) (2003) 633–636. doi:10.1126/science.1085048.

[43] Z. Guo, C. Zheng, B. Shi, Discrete lattice effects on the forcing term in the lattice Boltzmann method, Physical Review E 65 (2002) 046308. doi:10.1103/PhysRevE.65.046308.

[44] A. Anagnost, A. Alajbegovic, H. Chen, D. Hill, C. Teixeira, K. Molvig, Digital physics^{TM} analysis of the morel body in ground proximity, SAE transactions (1997) 306–312.

[45] D. Casalino, G. Romani, R. Zhang, H. Chen, Lattice-Boltzmann calculations of rotor aeroacoustics in transitional boundary layer regime, Aerospace Science and Technology 130 (2022) 107953. doi:10.1016/j.ast.2022.107953.

[46] D. Casalino, G. Romani, L. M. Pil, R. Colombo, Sensitivity of laminar separation noise from a rotor to inflow turbulence, AIAA AVIATION Forum (2023). doi:10.2514/6.2023-3220.

[47] Q. Zou, X. He, On pressure and velocity boundary conditions for the lattice Boltzmann BGK model, Physics of Fluids 9 (6) (1997) 1591–1598. doi:10.1063/1.869307.

[48] H. Chen, C. Teixeira, K. Molvig, Realization of fluid boundary conditions via discrete boltzmann dynamics, International Journal of Modern Physics C 09 (08) (1998) 1281–1292. doi:10.1142/S0129183198001151.

[49] Y. Li, An improved volumetric LBM boundary approach and its extension for sliding mesh simulation, Ph.D. thesis, Iowa State University (2012).
URL `https://dr.lib.iastate.edu/entities/publication/072bf03b-62ab-4307-8d00-79f9257cfc78`

[50] R. Zhang, C. Sun, Y. Li, R. Satti, R. Shock, J. Hoch, H. Chen, Lattice boltzmann approach for local reference frames, Communications in Computational Physics 9 (5) (2011) 1193–1205. doi:10.4208/cicp.021109.111110s.

[51] W. Z. Shen, R. Mikkelsen, J. N. Sørensen, C. Bak, Tip loss corrections for wind turbine computations, Wind Energy 8 (4) (2005) 457–475. doi:10.1002/we.153.

[52] J. N. Sørensen, K. Nilsson, S. Ivanell, H. Asmuth, R. F. Mikkelsen, Analytical body forces in numerical actuator disc model of wind turbines, Renewable Energy 147 (2020) 2259–2271. doi:10.1016/j.renene.2019.09.134.

[53] K. O. Dağ, J. N. Sørensen, A new tip correction for actuator line computations, Wind Energy 23 (2) (2020) 148–160. doi:10.1002/we.2419.

[54] A. R. Meyer Forsting, G. R. Pirrung, N. Ramos-García, A vortex-based tip/smearing correction for the actuator line, Wind Energy Science 4 (2) (2019) 369–383. doi:10.5194/wes-4-369-2019.

[55] M. Shives, C. Crawford, Mesh and load distribution requirements for actuator line CFD simulations, Wind Energy 16 (8) (2013) 1183–1196. doi:10.1002/we.1546.

[56] M. J. Churchfield, S. J. Schreck, L. A. Martinez, C. Meneveau, P. R. Spalart, An advanced actuator line method for wind energy applications and beyond, 35th Wind Energy Symposium (2017). doi:10.2514/6.2017-1998.

[57] V. G. Kleine, A. Hanifi, D. S. Henningson, Simulating airplane aerodynamics with body forces: Actuator line method for nonplanar wings, AIAA Journal 61 (5) (2023) 2048–2059. doi:10.2514/1.J062398.

[58] J. Nathan, C. Masson, L. Dufresne, Near-wake analysis of actuator line method immersed in turbulent flow using large-eddy simulations, Wind Energy Science 3 (2) (2018) 905–917. doi:10.5194/wes-3-905-2018.

[59] A. R. M. Forsting, N. Troldborg, Generalised grid requirements minimizing the actuator line angle-of-attack error, Journal of Physics: Conference Series 1618 (5) (2020) 052001. doi:10.1088/1742-6596/1618/5/052001.

[60] M. Drela, XFOIL: An analysis and design system for low Reynolds number airfoils, in: T. J. Mueller (Ed.), Low Reynolds Number Aerodynamics, Springer Berlin Heidelberg, Berlin, Heidelberg, 1989, pp. 1–12. doi:10.1007/978-3-642-84010-4_1.

[61] M. S. Selig, C. A. Lyon, P. Giguere, C. P. Ninham, J. J. Guglielmo, Summary of Low-Speed Airfoil Data, Volume 2, SoarTech Publications, 1996.
URL `https://m-selig.ae.illinois.edu/uiuc_lsat/Low-Speed-Airfoil-Data-V2.pdf`

[62] J. N. Sørensen, K. O. Dag, N. Ramos-García, A refined tip correction based on decambering, Wind Energy 19 (5) (2016) 787–802. doi:10.1002/we.1865.

[63] J. M. Delery, Aspects of vortex breakdown, Progress in Aerospace Sciences 30 (1) (1994) 1–59. doi:10.1016/0376-0421(94)90002-7.

[64] N. M. Chaderjian, Advances in rotor performance and turbulent wake simulation using des and adaptive mesh refinement, in: Seventh International Conference on Computational Fluid Dynamics (ICCFD7), 2012. URL https://ntrs.nasa.gov/api/citations/20130001604/downloads/20130001604.pdf

[65] P. Weihing, M. Cormier, T. Lutz, E. Krämer, The near-wake development of a wind turbine operating in stalled conditions – part 1: Assessment of numerical models, Wind Energy Science 9 (4) (2024) 933–962. doi:10.5194/wes-9-933-2024.